

Magnetic properties of strained $\text{La}_{2/3}\text{Sr}_{1/3}\text{MnO}_3$ perovskites from first principles

D Böttcher^{1,2} and J Henk²

¹ Max-Planck-Institut für Mikrostrukturphysik, Weinberg 2, D-06120 Halle (Saale), Germany

² Institut für Physik, Martin-Luther-Universität Halle-Wittenberg, D-06120 Halle (Saale), Germany

E-mail: dboettch@mpi-halle.de

Received 12 October 2012, in final form 29 January 2013

Published 7 March 2013

Online at stacks.iop.org/JPhysCM/25/136005

Abstract

The critical temperature T_C of ferromagnetic $\text{La}_x\text{Sr}_{1-x}\text{MnO}_3$ (LSMO) can be controlled by distorting the crystal structure, as was reported by Thiele *et al* (2007 *Phys. Rev. B* **75** 054408). To confirm these findings theoretically, we investigate the electronic as well as the magnetic ground state properties of $\text{La}_{2/3}\text{Sr}_{1/3}\text{MnO}_3$ as a function of tetragonal lattice distortions, using a multiple-scattering Green function method. Within this approach, we calculate exchange coupling constants as well as the phase transition temperature from first principles. Comparing our findings with those for $\text{La}_{2/3}\text{Sr}_{1/3}\text{CoO}_3$ (LSCO), we find that the decrease of T_C is much stronger in LSMO than in LSCO. Our findings can be explained by the electronic structures and are also in accordance with the experiment. The computed decrease of T_C with distortion is smaller than observed experimentally, a result that corroborates the importance of phonon contributions.

(Some figures may appear in colour only in the online journal)

1. Introduction

Multiferroic materials offer a broad spectrum of applications [1–3]. In some systems, a coupling between the crystal structure and ferromagnetism or ferroelectricity shows up. For example, the Piezoelectric effect generates an electric polarization by distortion of the crystal lattice. Likewise, lattice strain can change magnetic properties [4].

Perovskites are representatives for materials that show the above effects [5–10]. Especially, perovskitic oxides exhibit a variety of crystallographic, electronic as well as magnetic properties that can be controlled by chemical decomposition as well as by strain. Since the mid-20th century, perovskitic manganites, which exhibit high magnetic phase transition temperatures, have been spotlighted [11] and applied in tunnel contacts. $\text{La}_{2/3}\text{Sr}_{1/3}\text{MnO}_3$ (LSMO) lends support for such applications because of its coherent growth of monocrystalline layers [12, 13]. A LSMO/STO/LSMO tunnel contact, where STO stands for SrTiO_3 , shows a spin polarization as large as 95% and a magnetoresistance as large

as 1800% [14] at $T = 4.2$ K; with increasing temperature this effect disappears, which is explained by a reduced stability of the ferromagnetic order due to structural distortions [15, 16].

A similar instability of ferromagnetic order due to lattice distortion was also reported by Thiele *et al* [17]. The exchange coupling and the associated phase transition temperature in ferromagnetic LSMO can change by unexpectedly large amounts due to small tetragonal crystal distortions. Starting from an initial strain of 1%, a subsequent distortion of 0.1% decreases the Curie temperature by about 19 K. Hence, the effective change is as large as $\partial T_C = 190$ K/%. This effect is theoretically not well understood yet, to our knowledge, and calls for an investigation within the framework of first-principles calculations.

To calculate the electronic and magnetic ground state properties in a strained crystal lattice, a scalar-relativistic multiple-scattering Green function approach (the Korringa–Kohn–Rostoker method) has been used. We calculate Heisenberg exchange coupling constants, from which the critical temperature is obtained within the

mean-field approximation, the random phase approximation (RPA), as well as by Monte Carlo simulations. We compare the results for LSMO with those for $\text{La}_{2/3}\text{Sr}_{1/3}\text{CoO}_3$ (LSCO), for which a reduced effect has been found in experiment.

Our calculations reproduce the trends found in the experiment by Thiele *et al* [17] on both LSMO and LSCO. However, the differential changes in the critical temperatures are significantly too small. This finding suggests that electronic effects alone cannot explain the effect; we thus conclude that in addition phonon contributions may be important [18, 19].

The paper is organized as follows. Computational details are given in section 2. The magnetic and electronic properties of undistorted LSMO as well as of LSCO, which serves as a reference system, are addressed in section 3. The effect of tetragonal lattice distortions on the ground state properties for both perovskites are reported in section 4.

2. Computational aspects

Electronic ground state calculations have been performed by a scalar-relativistic Korringa–Kohn–Rostoker (KKR) method [20] that relies on the local spin-density approximation (LDA) to density functional theory. We utilize Perdew–Wang exchange correlation functionals [21–24] and apply the generalized gradient approximation (GGA) for LSMO, but the local spin-density approximation for LSCO. The choice of the exchange correlation functional affects mainly the magnetic atoms. Studies of the ground state of Co [25] and of Mn [26] show that experimental data are described well using LDA for Co and GGA for Mn.

Our approach is based on multiple-scattering theory, in which the electronic structure is described by scattering path operators τ_{ij} (i, j lattice site indices) [20]. In the spin-angular-momentum representation, we consider angular momenta up to $l_{\text{max}} = 3$. The substitutional alloys are treated within the coherent potential approximation (CPA). Sr impurities in the LMO host lattice are created in the effective CPA medium by defect matrices. The CPA medium is described by scattering path operators τ_{ij}^{cpa} .

The site-dependent potentials are taken as spherically symmetric within muffin-tin spheres and constant in the interstitials. Within the atomic sphere approximation (ASA), the atomic polyhedra are replaced by spheres of the same volume. Consequently, each muffin-tin radius equals the Wigner–Seitz radius, which guarantees identical volumes for the unit cell and for the sum of all potential spheres within the unit cell. As we discuss in detail below, this restriction of the potential shape introduces some arbitrariness in the calculations for distorted systems. For example, it turns out that the Wigner–Seitz radius for a La atom that is scaled by a factor of 0.7–0.8 reproduces both the experimental T_C and the magnetic moment. The scaling of the Wigner–Seitz radius provides simultaneously the best space filling factor and the smallest overlap of adjacent spheres.

Lattice distortions are considered by transformations of the lattice and the basis vectors. The structural relaxations of oxygen atoms have been neglected.

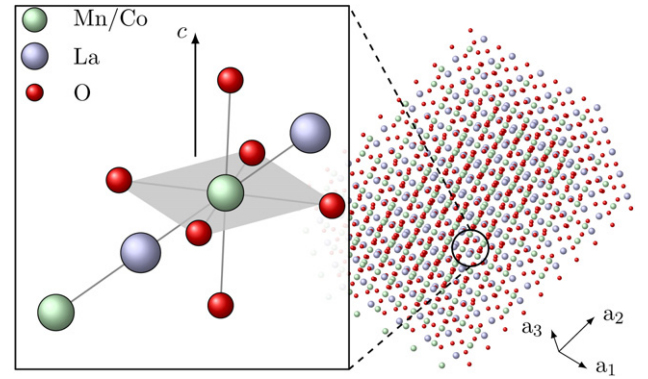


Figure 1. Sketch of a perovskite structure ABO_3 , $\text{B} = \text{Mn, Co}$. Each Mn or Co atom (green sphere) is surrounded by six oxygen atoms (red spheres). The z -axis defines the c -axis in the tetragonal case; the x - and y -axes span the a -plane (gray area spanned between the oxygen sites).

The Heisenberg exchange interactions J_{ij} are calculated from first principles using the aforementioned KKR method. For sites $i \neq j$ the exchange coupling constant is given by [27]

$$J_{ij} = \frac{1}{4\pi} \text{tr} \int^{E_F} \Delta \mathbf{t}_i \boldsymbol{\tau}_{ij}^\uparrow \Delta \mathbf{t}_j \boldsymbol{\tau}_{ji}^\downarrow dE, \quad (1)$$

with $\Delta \mathbf{t}_i \equiv \mathbf{t}_i^\uparrow - \mathbf{t}_i^\downarrow$. \mathbf{t}_i^σ and $\boldsymbol{\tau}_{ij}^\sigma$ are the spin-resolved KKR single-site scattering matrices and the scattering path matrices in the spin-angular-momentum representation ($\sigma = \uparrow, \downarrow$), respectively [20]. $\boldsymbol{\tau}_{ij}$ describes the propagation of an electron from site j to site i . The energy integral runs up to the Fermi energy E_F .

3. Crystal structure and ground state properties

Perovskite structures ABO_3 can exhibit an enlarged supercell with respect to their basic cubic form because of deviations from the 180° angles in the O–B–O bonds. To get a full *ab initio* description of the perovskitic systems, we take into account in this work these deviations.

Structures within the crystal group 167 are characterized by their fractional indices: $\text{A} = (0, 0, 0)$, $\text{B} = (\frac{1}{4}, \frac{1}{4}, \frac{1}{4})$, $\text{O} = (z, \frac{1}{2} - z, \frac{1}{4})$, where z varies among the perovskites. In the following, we focus on $\text{La}_{2/3}\text{Sr}_{1/3}\text{MnO}_3$ ($z = -0.29$) and $\text{La}_{2/3}\text{Sr}_{1/3}\text{CoO}_3$ ($z = 0.21$) (figure 1). In our calculations, the lattice constant is taken from experiment: $a = 5.47 \text{ \AA}$ [28] (Thiele *et al* found $a = 5.46 \text{ \AA}$ [7, 17]) for LSMO and $a = 5.39 \text{ \AA}$ [29] for LSCO.

LSMO and LSCO differ in their metallic behavior, which can be seen in the density of states (DOS; figure 2). LSMO manifests a band gap in the minority spin channel, thus indicating half-metallicity. Due to this gap, the exchange splitting and the magnetic moments are large ($M = 3.67 \mu_B$, experimental $M = 3.70 \mu_B$ [30]). In contrast, LSCO has fully occupied d states with majority spin. A peak in the minority spin appears at the Fermi level; hence, LSCO exhibits metallic character. The exchange splitting as well as the magnetic moments are smaller in comparison to LSMO ($M = 1.63 \mu_B$; experimental $M = 1.71 \mu_B$ [29]).

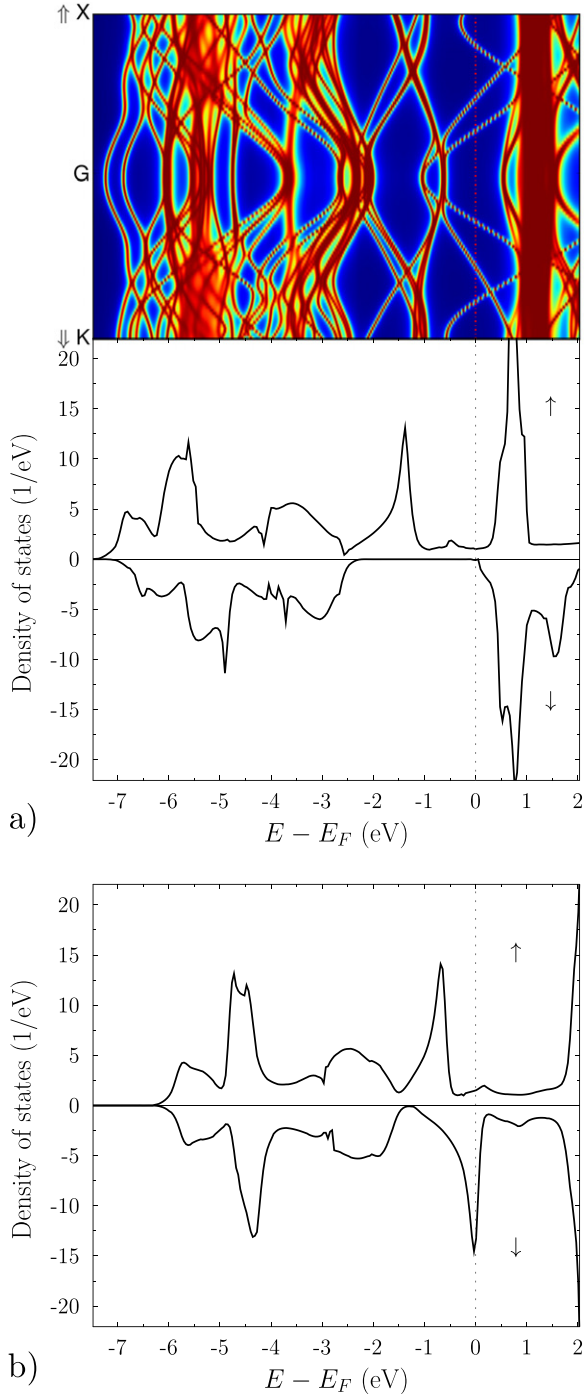


Figure 2. Spin-resolved electronic structure for (a) $\text{La}_{2/3}\text{Sr}_{1/3}\text{MnO}_3$ and (b) $\text{La}_{2/3}\text{Sr}_{1/3}\text{CoO}_3$ (minority spin \downarrow , majority spin \uparrow). In addition, the band structure of LSMO is shown in a small range around the center of the Brillouin zone, Γ ; the respective directions in reciprocal space, toward the high-symmetry points X and K, are indicated. E_F is the Fermi energy.

Due to the hybridization of electronic states associated with oxygen and the magnetic atoms (Mn or Co), oxygen sites carry a finite but negligibly small magnetic moment ($0.073 \mu_B$ in LSMO, $0.013 \mu_B$ in LSCO). Furthermore, the La and Sr magnetic moments are small as well ($0.12 \mu_B$ (La) and $0.043 \mu_B$ (Sr) in LSMO; $0.003 \mu_B$ (La) and $0.008 \mu_B$

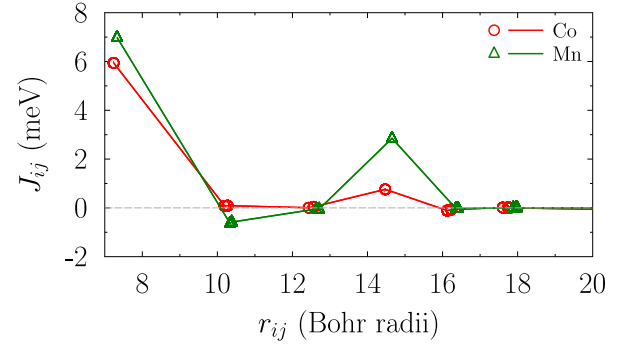


Figure 3. Heisenberg exchange coupling constants J_{ij} for Mn in LSMO (green, open triangles) and Co in LSCO (red, open circles) versus distance $r_{ij} \equiv |\mathbf{r}_i - \mathbf{r}_j|$ for sites i and j .

(Sr) in LSCO). Hence, the major contribution comes from the transition metal atoms (Mn, Co). As a consequence, we will consider exchange parameters J_{ij} only between these atoms (figure 3).

In contrast to LSCO, LSMO has a small antiferromagnetic (negative) second- and a significant fourth-nearest neighbor coupling contribution. Apart from that, the decay in the exchange coupling with distance r_{ij} is similar. The next-nearest neighbor coupling for LSMO and for LSCO calculated using equation (1) gives $J = 6.99$ meV and 5.94 meV, respectively. Within the random phase approximation, the Curie temperature is estimated to $T_C = 305$ K for LSMO (experiment 330 K [30]) and to 210.7 K for LSCO (experiment 227 K [29]). The agreement of both the critical temperature T_C and the magnetic moments with the experimental values supports the validity of our first-principles approach.

4. Lattice distortion

We now address the change of the magnetic characteristics (critical temperature, magnetic moments, and exchange splitting) with the tetragonal lattice distortion along the c -direction (figure 1).

Following the *ansatz* of Biegalski *et al* [31], the change of the in-plane lattice constant Δ' with respect to the out-of-plane lattice constant Δ reads as

$$\Delta' = \frac{1 - \mu}{2\mu} \Delta. \quad (2)$$

The Poisson number μ is defined as the ratio between the relative thickness and the length variation. For perovskitic structures, μ can be approximated by $1/3$ [31], which results in $\Delta' = \Delta$.

For a tetragonal distortion $\mathbf{r}' = \mathbf{D}\mathbf{r}$, the transformation matrix \mathbf{D} reads as

$$\mathbf{D} = \begin{pmatrix} 100 - \Delta' & 0 & 0 \\ 0 & 100 - \Delta' & 0 \\ 0 & 0 & 100 + \Delta \end{pmatrix}. \quad (3)$$

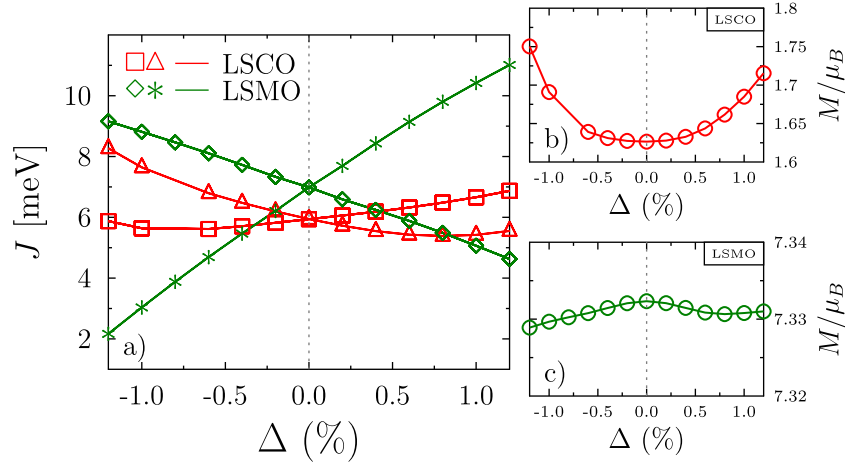


Figure 4. Nearest neighbor Heisenberg exchange parameters J (a) as well as the average magnetic moment M versus tetragonal volume-conserving lattice distortion Δ for LSMO ((b) green lines and symbols) and for LSCO ((c) red lines and symbols). The symbols in the figure on the left refer to the in-plane (squares, diamonds) and out-of-plane (triangles, asterisks) contributions.

This distortion does not conserve the volume (Δ and Δ' in %). To guarantee volume conservation, \mathbf{D} is modified to

$$\mathbf{D}_{vc} = \begin{pmatrix} u\sqrt{100 - \Delta} & 0 & 0 \\ 0 & u\sqrt{100 - \Delta} & 0 \\ 0 & 0 & u(100 + \Delta) \end{pmatrix}, \quad (4)$$

$$u = \left(1 - \Delta^2\right)^{-\frac{1}{3}},$$

where Δ is the distortion parameter in %. Volume conservation is often considered in studies of the magnetic stability [30]. Hence, we will first dedicate ourselves to this scenario (figure 4).

Half-metallic and metallic materials show different responses to the distortion of the crystal structure. On the one hand, half-metallic LSMO exhibits a constant magnetic moment. This is explained by the large band gap in the minority spin channel (figure 2) that is insensitive to Δ . Therefore, the n_{\downarrow} density of states is a well approximated constant. On the other hand, the magnetic moment of metallic LSCO is enhanced by about $0.06 \mu_B$ for $\Delta = 1\%$, which is consistent with a larger change in the minority spin density of states.

Under lattice strain, the exchange interaction becomes anisotropic. The nearest neighbor exchange parameters J split into an in-plane (figure 4, squares) and an out-of-plane (figure 4, triangles) branch. The slopes of these branches are larger (in absolute value) for LSMO than for LSCO. Furthermore, the J 's for LSMO behave strictly monotonically, whereas both J branches for LSCO increase for large distortions ($|\Delta| > 1\%$).

From these exchange interactions J we deduce the phase transition temperatures within the mean-field approximation (circles in figure 5) and the random phase approximation (triangles). The mean-field approach overestimates the Curie temperature by about 100 K, whereas the random phase approximation gives better agreement with experiment. The T_C 's for both LSMO and LSCO show parabolic behavior versus lattice distortion Δ . The curvatures are almost identical

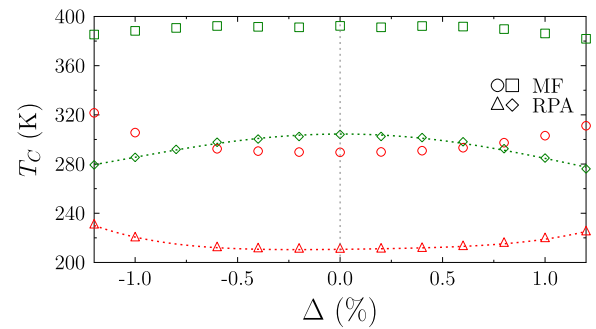


Figure 5. Curie temperature versus tetragonal volume-conserving lattice distortion for LSMO (green lines and symbols (squares, diamonds)) and for LSCO (red lines and symbols (circles, triangles)). The phase transition temperature is calculated within the mean-field (MF) approximation (circles, squares) and the random phase approximation (RPA, triangles, diamonds). The dashed lines are a polynomial of fourth order fitted to the RPA data. The slopes at $\Delta = \pm 1\%$ are 24.12 K/% and 36.67 K/% for LSCO and 34.60 K/% and 30.39 K/% for LSMO, respectively.

but the slopes show opposite sign. From a parabolic fit we estimate the effective change of the critical temperature ∂T_C (slope of the curve) at $\Delta = 1\%$; it is identical for both materials, namely $\partial T_C \approx 30$ K/%.

Distortions in theory that do not conserve the volume correlate better to the experiment, as we will now show for LSMO. Here, we consider LSCO mainly for comparison. The Poisson number μ affects the c/a -ratio; it therefore induces strong anisotropies within the crystal (contrary to the volume-conserving case). Hence, we consider two representative values for the Poisson number, $\mu = 3/5$ and $1/3$, where the latter is taken from experiment [32, 33] (figure 6).

Similar to the volume-conserving case, the magnetic moments in LSMO can be approximated as constant (not shown here). However, one obtains considerable differences between compression (figure 6 for $\Delta < 0\%$) and stretching (figure 6 for $\Delta > 0\%$). This finding is attributed to the

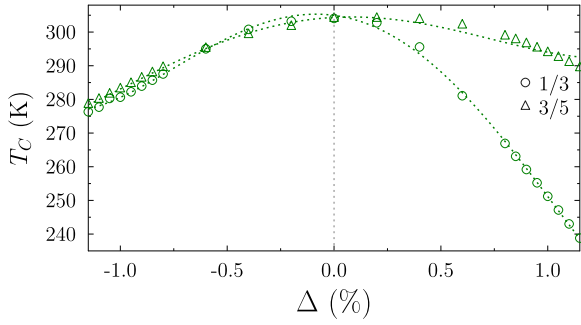


Figure 6. Curie temperature T_C versus tetragonal lattice distortion Δ in LSMO for two Poisson numbers, as indicated ($\mu = 3/5$ triangles; $\mu = 1/3$ circles). Lines represent a fitted polynomial of fourth order. The slopes at $\Delta = \pm 1\%$ are 84.10 K/% and 29.23 K/% for $\mu = 1/3$ and 12.26 K/% and 31.83 K/% for $\mu = 3/5$, respectively.

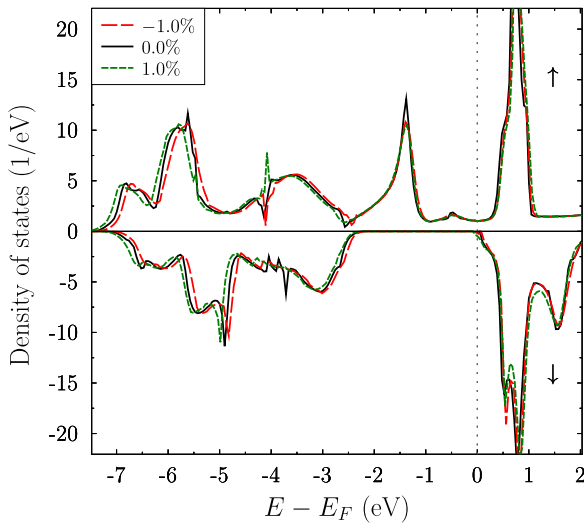


Figure 7. Spin-resolved electronic structure for distorted LSMO, as indicated (minority spin \downarrow , majority spin \uparrow). E_F is the Fermi energy. The Poisson number is $\mu = 1/3$.

differences in coordination for in- and out-of-plane neighbors in LSMO and the different Poisson numbers. It is traced back to the electronic structure near the Fermi energy (figures 7 and 8).

The spin-down channel in the density of states is more affected by the distortion than the spin-up channel (figure 7). If the c/a ratio is larger than 1 ($\Delta > 0$), electronic states in the spin-down channel near the Fermi level become occupied. This rearrangement reduces the exchange splitting and results, in a Stoner picture, in a decreased phase transition temperature. In contrast, for $c/a < 1$ ($\Delta < 0$), mainly a repopulation of electronic states at lower energies takes place, which does not affect significantly the Curie temperature.

Due to distortion, the crystal symmetry is reduced. The associated change in the crystal field modifies the d levels (especially the e_g levels, which are located below the Fermi level and up to 1 eV, and the t_{2g} levels, located below 1 eV) in the band structure, e.g. around Γ (figure 8). For stretching (figure 8(b)), an initially unoccupied band crosses

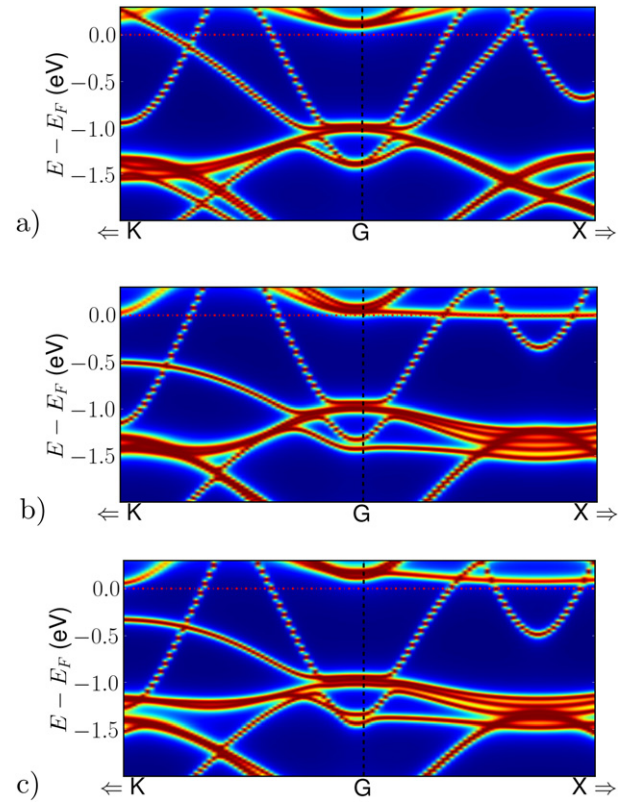


Figure 8. Band structure for distorted LSMO in a small region around the center of the Brillouin zone, Γ , for (a) $\Delta = 0\%$, (b) $\Delta = 1\%$, and (c) $\Delta = -1\%$. The directions in the Brillouin zone (toward the high-symmetry points K and X), starting from Γ , are marked by arrows.

the Fermi level. It is populated by minority spin electrons and consequently modifies the magnetic properties. In contrast to compression (figure 8(c)), these states do not cross the Fermi level. This difference is in line with the different slopes for T_C versus Δ . Considering the charge state of the atoms, we observe a transfer of electrons (less than 0.05 electrons within the muffin-tin spheres) from Sr, La and Mn to the oxygen atoms in the entire range of lattice strain. Hence, the valency of Mn and Co remains unchanged upon distortion.

The Mn atoms in undistorted LSMO couple ferromagnetically, with a J of 6.9 meV. Stretching the structure in the c -direction ($\Delta > 0$) increases the ferromagnetic coupling between Mn atoms that are displaced parallel to c (for $\Delta = 1\%$ and $\mu = \frac{1}{3}$, $J = 1.19$ meV). However, the in-plane ferromagnetic coupling becomes weaker ($\Delta = 1\%$ and $\mu = \frac{1}{3}$, $J = 3.70$ meV) and can actually turn into antiferromagnetic coupling (negative J at about $\Delta = 2\%$). The effective interaction parameter, which is defined as the sum over all J 's of the magnetic nearest and, for the case of a strained system, next-nearest neighbors, decreases (from $J_{\text{eff}} = 41.92$ meV in the undistorted case to $J_{\text{eff}} = 37.18$ meV in the distorted case ($\Delta = 1\%$)). Loosely speaking, the system acquires a ‘more antiferromagnetic’ character, which is in accordance with the Goodenough–Kanamori–Anderson rules [34–36].

Upon compression along the c -axis, the system shows the reverse effect. The out-of-plane interaction decreases

($\Delta = -1\%$ and $\mu = 1/3$ give $J = 1.45$ meV) and becomes antiferromagnetic at $\Delta = 1.9\%$, since the in-plane contribution increases ($\Delta = -1\%$ and $\mu = 1/3$ give $J = 9.46$ meV). The change in the magnetic coupling is weaker with respect to $\Delta > 0$; the effective interaction parameter is reduced less (from $J_{\text{eff}} = 41.92$ meV in the undistorted case to $J_{\text{eff}} = 41.85$ meV in the distorted case ($\Delta = -1\%$)). Similarly for the volume-conserving case, two branches with different slopes occur, one for the in-plane and one for the out-of-plane interaction (not shown here).

For the Poisson number $\mu = 3/5$, the reduction of the Curie temperature with respect to the undistorted case is smaller than for $\mu = 1/3$, which is attributed to a reduced change in the in-plane and the out-of-plane interaction parameters. Because of this, the difference between the effective interactions in the undistorted and distorted state is less with respect to the previous case; the correlation of T_C versus Δ is almost symmetric around zero.

Our calculations yield more or less the order of magnitude of the experimental $\partial T_C = 190$ K/%. Considering $\mu = 1/3$, we observe a negative $\Delta \partial T_C = 30$ K/% (too small by a factor of 6) and a positive $\Delta \partial T_C = 80$ K/% (too small by a factor of 2). This raises the question as to the effect of a particular critical parameter in our approach, namely the Wigner–Seitz radius that has been optimized to reproduce the critical temperature of undistorted LSMO.

For lanthanides, the overlap between neighboring muffin-tin potentials is important for a correct description of the magnetic structure. Däne has studied this effect on lanthanides for different c/a ratios and for different sphere volumes [37]. For a constant c/a ratio, the magnetic order turns from an incommensurable spin structure into ferromagnetic order upon increasing the volume. Also for a change in the c/a ratio at constant volume, a transition from ferromagnetic order to an incommensurable spin structure occurs. This finding is supported by experiments on terbium [38].

The approximation of the potential shape by a sphere may not be appropriate in the case of a distorted lattice; here, an ellipsoidal shape could be better. However, it is very hard and beyond the scope of this paper to develop a multiple-scattering theory with ellipsoids rather than with spheres. Therefore, we introduce a scaling of the Wigner–Seitz radius with Δ .

The radius is expressed as $r'_{\text{WS}} = \sigma_{\text{WS}} r_{\text{WS}}$. $r_{\text{WS}} = 3.48$ Bohr radii is the calculated initial value; a fit to the experiment for the nondistorted case yields $\sigma_{\text{WS}} = 0.8$. We now address the dependency of T_C on σ_{WS} for the distorted lattice (figure 9).

The linear correlation of $T_C(\sigma_{\text{WS}})$ exhibits a strong dependency on σ_{WS} . ∂T_C at constant σ_{WS} (figure 9, inset) indicates that the experimental value for $\partial T_C = 190$ K/% is not reproduced with a constant scaling factor. Hence, we assume that σ_{WS} depends linearly on Δ . If the difference in the T_C 's for Δ and for Δ equals the experimental value, we obtain the relation $\sigma'_{\text{WS}} = \frac{\Delta \sigma_{\text{WS}}}{\Delta - \Delta} (1 + \Delta)$ for a linear transformation, with $\Delta \sigma_{\text{WS}} = 0.05913 \sigma_{\text{WS}}^i - 0.01906$; here, σ_{WS}^i is a fitting parameter (for $\sigma_{\text{WS}}^i = 0.81$ one arrives at $\Delta \sigma_{\text{WS}} = 0.029$). This relation provides an unphysically large scaling factor; only with a very large overlap, which implies a long-range

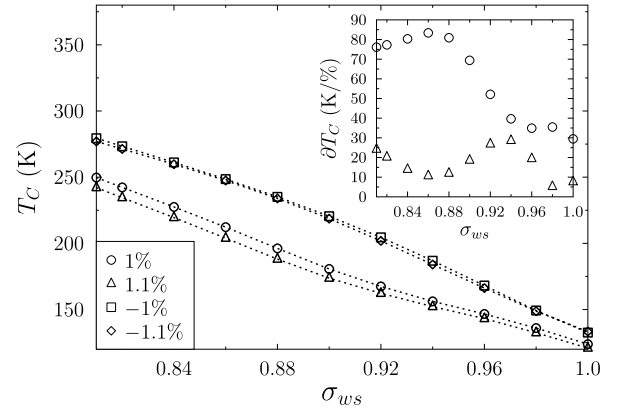


Figure 9. Critical temperature T_C versus scaling factor σ_{WS} of the Wigner–Seitz radius in bulk LSMO for different distortions, as indicated. Dotted lines are guides to the eye. The inset shows the effective phase transition change ∂T_C versus σ_{WS} for $\Delta > 0$ (circles) and for $\Delta < 0$ (triangles).

effect of the potentials, does the experimental trend become reproducible.

The analysis above shows that first-principles calculations on the electronic and the magnetic structure explain the experimental trends in LSMO and LSCO but there are difficulties in reproducing the exact numbers. This observation suggests that the calculations do not account for the additional effects that are needed for a complete explanation. First, lattice vibrations could increase the differential change in the Curie temperature [39, 40]: The electron–phonon coupling leads to the occupation of electronic states slightly above the Fermi level, which affects the exchange splitting and hence the Curie temperature. The density of states suggests that LSMO is sensitive to such a population of electronic states. Second, the temperature-dependent variation of the lattice constant in the c -direction has been studied by May *et al* [6]. The lattice distortion in the c -direction is increased by 0.5% by temperature. According to our calculations, this results in an increased change of the Curie temperature by about 16 K, thus leading to better agreement with the experimental value. Third, on the experimental side, one could think about deducing the experimental values for ∂T_C with increased accuracy. At present, these numbers have been derived from a fitting and extrapolation procedure for $M^2(T)$ in [17]. Fourth, the shortcomings of the muffin-tin approximation could be overcome by a full-potential approach [41]. However, this is computationally very demanding. Instead, we performed calculations within the full charge-density approximation [42], a quasi-full-potential approach, for selected setups; we found no significant changes compared to the reported muffin-tin results. Wavefunction based methods, like pseudopotential plane-wave or projector augmented-wave approaches [43–50], do not rely on shape approximations for the potential and, thus, could yield better results. However, chemical disorder has to be treated within a supercell approach which may introduce other problems (e.g. artificial effects of short-range order by too small a supercell).

To support our approach further, we compare LSMO with LSCO (figure 10) for a Poisson number of 3/5 in

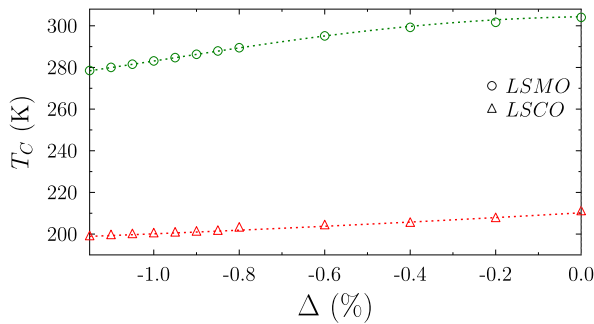


Figure 10. Curie temperature T_C versus lattice distortion Δ for LSMO (green) and for LSCO (red). The calculated data are fitted by a polynomial of fourth order (dotted lines). The slopes at a distortion of $\Delta = -1\%$ are calculated from the derivative of the polynomial and are 31.83 K/% for LSMO and 8.39 K/% for LSCO.

the experimentally relevant region ($\Delta < 0$). A fourth-order polynomial fit gives a value of ∂T_C for LSCO that is one third as large as that for LSMO (LSMO $\partial T_C = 31.83$ K/%; LSCO $\partial T_C = 8.39$ K/%). The electronic structure is affected as well but not as strongly as in LSMO because the minority states are already occupied, in contrast to LSMO. These findings reproduce the experimental trends [17, 29].

5. Conclusion

The unexpectedly large change of the Curie temperature for $\text{La}_{2/3}\text{Sr}_{1/3}\text{MnO}_3$ upon lattice distortion, as reported in [17], is a feature of its half-metallicity, as is supported by our detailed first-principles calculations. Analogous computations for metallic $\text{La}_{2/3}\text{Sr}_{1/3}\text{CoO}_3$ show a considerably reduced change, in agreement with experiment. Our findings also suggest that electron–phonon coupling could be essential for the explanation of the effect [18, 19].

Our investigation is another step toward a comprehensive theoretical description of distorted $\text{La}_{2/3}\text{Sr}_{1/3}\text{MnO}_3$. Multiple-scattering theory, used in this work, is the method of choice for dealing with magnetic substitutional alloys but has the drawback of approximating the crystal potential by arrangements of spheres³. In contrast, full-potential approaches, like the full-potential linearized augmented plane-wave method, have in principle no shape approximation for the potential but in turn cannot deal well with substitutional alloys. Hence, distorted $\text{La}_{2/3}\text{Sr}_{1/3}\text{MnO}_3$ remains a challenge for first-principles electronic structure calculations.

Acknowledgments

This work is supported by the *Sonderforschungsbereich* 762 ‘Functional Oxide Interfaces’. DB is a member of the International Max Planck Research School on Science and Technology of Nanostructures, Halle, Germany. We gratefully

³ There are full-potential variants of multiple-scattering theory that are, however, extremely time-consuming. Also it appears to us that there is no coherent potential approximation for these flavors of the Korringa–Kohn–Rostoker method.

acknowledge fruitful discussions with Arthur Ernst, Igor Maznichenko and Kathrin Dörr.

References

- [1] Nan C-W, Bichurin M I, Dong S, Viehland D and Srinivasan G 2008 Multiferroic magnetoelectric composites: historical perspective, status, and future directions *J. Appl. Phys.* **103** 031101
- [2] Gajek M, Bibes M, Fusil St, Bouzouane K, Fontcuberta J, Barthélémy A and Fert A 2007 Tunnel junctions with multiferroic barriers *Nature Mater.* **6** 296
- [3] Binek Ch and Doudin B 2005 Magnetoelectronics with magnetoelectrics *J. Phys.: Condens. Matter* **2** L39–44
- [4] Spaldin N and Fiebig M 2005 The renaissance of magnetoelectric multiferroics *Science* **309** 5733
- [5] Xie C K, Budnick J I, Hines W A, Wells B O and Woicik J C 2008 Strain-induced change in local structure and its effect on the ferromagnetic properties of $\text{La}_{0.5}\text{Sr}_{0.5}\text{CoO}_3$ thin films *Appl. Phys. Lett.* **93** 182507
- [6] May S J *et al* 2009 Enhanced ordering temperatures in antiferromagnetic manganite superlattices *Nature Mater.* **8** 892–7
- [7] Souza-Neto N M, Ramos A Y and Tolentino H C 2004 Local tetragonal distortion in $\text{La}_{0.7}\text{Sr}_{0.3}\text{MnO}_3$ strained thin films probed by x-ray absorption spectroscopy *Phys. Rev. B* **70** 174451
- [8] Hwang H Y, Palstra T T M, Cheong S-W and Batlogg B 1995 Pressure effects on the magnetoresistance in doped manganese perovskites *Phys. Rev. B* **52** 21
- [9] Radaelli P G, Iannone G, Marezio M, Hwang H Y, Cheong S-W, Jorgensen J D and Argyriou D N 1997 Structural effects on the magnetic and transport properties of perovskite $\text{A}_{1-x}\text{A}'_x\text{MnO}_3$ ($x = 0.25, 0.30$) *Phys. Rev. B* **56** 13
- [10] May S J, Kim J-W, Rondinelli J M, Karapetrova E, Spaldin N A, Bhattacharya A and Ryan P J 2010 Quantifying octahedral rotations in strained perovskite oxide films *Phys. Rev. B* **82** 014110
- [11] Dörr K 2006 Ferromagnetic manganites: spin-polarized conduction versus competing interactions *J. Phys. D: Appl. Phys.* **39** R125–50
- [12] Kawasaki M, Izumi M, Konishi Y, Manako T and Tokura Y 1999 Perfect epitaxy of perovskite manganite for oxide spin-electronics *Mater. Sci. Eng. B* **63** 49–57
- [13] Koubaa A M, Haghiri-Gosnet M, Desfeux R, Lecoer P, Prellier W and Mercey B 2003 Crystallinity, surface morphology, and magnetic properties of $\text{La}_{0.7}\text{Sr}_{0.3}\text{MnO}_3$ thin films: an approach based on the laser ablation plume range models *J. Appl. Phys.* **93** 5227–35
- [14] Brown M, Bibes M, Barthélémy A, Contour J-P, Anane A, Lemaître Y and Fert A 2003 Nearly total spin polarization in $\text{La}_{2/3}\text{Sr}_{1/3}\text{MnO}_3$ from tunneling experiments *Appl. Phys. Lett.* **82** 233–5
- [15] Pailloux F, Imhoff D, Sikora T, Barthélémy A, Maurice J-L, Contour J-P, Colliex C and Fert A 2002 Nanoscale analysis of $\text{SrTiO}_3/\text{La}_{2/3}\text{Sr}_{1/3}\text{MnO}_3$ interface *Phys. Rev. B* **66** 014417
- [16] Millis A J 1998 Lattice effects in magnetoresistive manganese perovskites *Nature* **392** 147–50
- [17] Thiele C, Dörr K, Bilani O, Rödel J and Schultz L 2007 Influence of strain on the magnetization and magnetoelectric effect in $\text{La}_{0.7}\text{A}_{0.3}\text{MnO}_3/\text{PMN-PT}(001)$ ($A = \text{Sr}, \text{Ca}$) *Phys. Rev. B* **75** 054408
- [18] Krempaský J 2008 Angle- and spin-resolved photoemission on $\text{La}_{2/3}\text{Sr}_{1/3}\text{MnO}_3$ *PhD Thesis* Université de Cergy-Pontoise
- [19] Sun Z *et al* 2006 Quasiparticlelike peaks, kinks, and electron–phonon coupling at the $(\pi, 0)$ regions in the CMR oxide $\text{La}_{2-2x}\text{Sr}_{1+2x}\text{Mn}_2\text{O}_7$ *Phys. Rev. Lett.* **97** 056401

- [20] Zabloudil J, Hammerling R, Szunyogh L and Weinberger P (ed) 2005 *Electron Scattering in Solid Matter* (Berlin: Springer)
- [21] Langreth D C and Mehl M J 1983 Beyond the local-density approximation in calculations of ground-state electronic properties *Phys. Rev. B* **28** 1809
- [22] Becke A D 1988 Density-functional exchange-energy approximation with correct asymptotic behavior *Phys. Rev. A* **38** 3098
- [23] Perdew J P and Wang Y 1992 Accurate and simple analytic representation of the electron–gas correlation energy *Phys. Rev. B* **45** 13244
- [24] Perdew J P, Chevary S H, Vosko S H, Jackson K A, Pederson M R, Singh D J and Fiolhais C 1993 Erratum: atoms, molecules, solids, and surfaces: applications of the generalized gradient approximation for exchange and correlation *Phys. Rev. B* **48** 4978 (erratum)
- [25] Paxton A T, Methfessel M and Polatoglou M H 1990 Structural energy–volume relations in first-row transition metals *Phys. Rev. B* **41** 8127–38
- [26] Asada T and Terakura K 1993 Generalized-gradient-approximation study of the magnetic and cohesive properties of bcc, fcc, and hcp Mn *Phys. Rev. B* **47** 15992–5
- [27] Liechtenstein A I, Katsnelson M I, Antropov V P and Gubanov V A 1987 Local spin density functional approach to the theory of exchange interactions in ferromagnetic metals and alloys *J. Magn. Magn. Mater.* **67** 65
- [28] Trukhanov S V, Troyanchuk I O, Bobrikov I A, Simkin V G and Balagurov A M 2007 Structure phase separation in the anion-deficient $\text{La}_{0.70}\text{Sr}_{0.30}\text{MnO}_{3-\delta}$ manganite system *J. Surf. Invest.: X-ray, Synchrotron Neutron Tech.* **1** 705–10
- [29] Caciuffo R, Rinaldi D, Barucca G, Mira J, Rivas J, Senaris-Rodriguez M A, Radaelli P G, Fiorani D and Goodenough J B 1999 Structural details and magnetic order of $\text{La}_{1-x}\text{Sr}_x\text{CoO}_3$ ($x \leq 0.3$) *Phys. Rev. B* **59** 2
- [30] Ziese M *et al* 2010 Tailoring magnetic interlayer coupling in $\text{La}_{0.7}\text{Sr}_{0.3}\text{MnO}_3/\text{SrRuO}_3$ superlattices *Phys. Rev. Lett.* **104** 167203
- [31] Biegalski M D, Dörr K, Kim D H and Christen H M 2010 Applying uniform reversible strain to epitaxial oxide films *Appl. Phys. Lett.* **96** 151905
- [32] Ranno L, Llobet A, Tiron R and Favre-Nicolin E 2002 Strain-induced magnetic anisotropy in epitaxial manganite films *Appl. Surf. Sci.* **188** 170–5
- [33] Maurice J-L, Pailloux F, Barthélémy A, Durand O, Imhoff D, Lyonnet R, Rocher A and Contour J-P 2003 Strain relaxation in epitaxy of $\text{La}_{2/3}\text{Sr}_{1/3}\text{MnO}_3$ grown by pulsed laser deposition in $\text{SrTiO}_3(001)$ *Phil. Mag.* **83** 3201–24
- [34] Goodenough J B 1955 Theory of the role of covalence in the perovskite-type manganites (La, M(II)) MnO_3 *Phys. Rev.* **100** 564–73
- [35] Kanamori J 1959 Superexchange interaction and symmetry properties of electron orbitals *J. Phys. Chem. Solids* **10** 87
- [36] Anderson P W, Seitz F and Turnbull D 1963 Theory of magnetic exchange interaction: exchange in insulators and semiconductors *Solid State Phys.* **14** 99–214
- [37] Däne M 2008 Beschreibung der elektronischen Struktur korrelierter Systeme mittels lokaler Selbstwechselwirkungskorrekturen im Rahmen der Vielfachstreuungstheorie *PhD Thesis* Martin-Luther-Universität Halle-Wittenberg
- [38] Andrianov A V I, Kosarev D I and Beskrovnyi A I 2000 Helical magnetic ordering in Tb completely suppressed by uniaxial tension: evidence of electronic topological transition and support for the nesting hypothesis *Phys. Rev. B* **62** 13844–7
- [39] Viswanathan M, Kumar P S, Bhadrani V S, Narayana C, Bera A K and Yusuf S M 2010 Influence of lattice distortion on the Curie temperature and spin–phonon coupling in $\text{LaMn}_{0.5}\text{Co}_{0.5}\text{O}_3$ *J. Phys.: Condens. Matter* **22** 346006
- [40] Chan N N 1990 The shift of the Curie temperature due to spin–phonon interaction *Czech. J. Phys.* **40** 341–4
- [41] Hatada K, Hayakawa K, Benfatto M and Natoli C R 2010 Full-potential multiple scattering theory with space-filling cells for bound and continuum states *J. Phys.: Condens. Matter* **22** 185501
- [42] Vitos L, Kollar J and Skriver H L 1994 Full charge-density calculation of the surface energy of metals *Phys. Rev. B* **49** 23
- [43] Delin A and Tosatti E 2003 Magnetic phenomena in 5d transition metal nanowires *Phys. Rev. B* **68** 144434
- [44] Delin A and Tosatti E 2004 The electronic structure of 4d transition-metal monatomic wires *J. Phys.: Condens. Matter* **16** 8061
- [45] Spišák D and Hafner J 2002 Fe nanowires on vicinal Cu surfaces: *ab initio* study *Phys. Rev. B* **65** 235405
- [46] Kresse G and Hafner J 1993 *Ab initio* molecular dynamics for liquid metals *Phys. Rev. B* **47** 558
- [47] Kresse G and Hafner J 1994 *Ab initio* molecular-dynamics simulation of the liquid–metal–amorphous–semiconductor transition in germanium *Phys. Rev. B* **49** 14251
- [48] Kresse G and Furthmüller J 1996 Efficient iterative schemes for *ab initio* total-energy calculations using a plane-wave basis set *Phys. Rev. B* **54** 11169
- [49] Kresse G and Joubert D 1999 From ultrasoft pseudopotentials to the projector augmented-wave method *Phys. Rev. B* **59** 1758
- [50] Blöchl P E 1994 Projector augmented-wave method *Phys. Rev. B* **50** 17953